https://doi.org/10.1038/s44310-025-00089-y

Imaging-based quantification of sub-25 nm coking layer on Au by dielectric-loaded plasmonic azimuthally chirped gratings

Yi-Ju Chen[1] ✉, Abhik Chakraborty[1,2], Tzu-Heng Chen[1,3], Sahitya Varma Vegesna[1,4], Heidemarie Krüger[1,4], Uwe Hübner[1] & Jer-Shing Huang[1,2,5,6] ✉

Noble metals are commonly used in heterogeneous catalysis due to their active catalytic sites. However, carbon layer deposition, or coking, can block these sites and reduce performance, even at thicknesses below 25 nm. Rapid monitoring of ultrathin coking layers is therefore essential for timely surface renewal and sustained catalytic efficiency. Conventional analysis methods are expensive, destructive, require bulky instruments, and lack in-situ, real-time capabilities. In this work, we present a simple, image-based optical method for non-destructive monitoring of sub-25 nm coking layers. This approach uses direct imaging of dielectric-loaded plasmonic azimuthally chirped gratings (DL-pACGs) on the coked gold surface, where reflection images reveal azimuthal dark bands from plasmon coupling. The position of these bands correlates with carbon thickness, enabling quantitative analysis. Ellipsometry data from thin carbon films were incorporated into simulations, showing strong agreement with experimental results. This method is simple, effective, and non-destructive for quantifying thin coke films.

Noble metal catalysts are widely used in heterogeneous catalysis, including organic synthesis[1–3], carbon dioxide reduction[4–6], catalytic converters[7–9], and fuel cells[10–12]. However, these catalytic reactions often suffer from issues such as poisoning, aging, coking or fouling on the metal surface, which significantly impair catalytic activity and stability[13,14]. The presence of coke, for instance, can block active sites and impede heat transfer, leading to decreased catalyst performance and requiring replacement or reactivation[13]. The typical thickness of the coking layer formed on noble metal electrodes during catalytic chemical reactions can vary depending on factors such as reaction conditions, catalyst material, the type of coke formed, and operating time. Carbon deposits on metal catalyst surfaces can range from a few nanometers to several micrometers, depending on the extent of coking and the reaction environment. Studies have shown that even an ultra-thin coke layer with a thickness of less than 25 nm is sufficient to block active sites, thereby reducing catalytic efficiency[15–17].

To overcome these issues, it is beneficial to monitor the coke load on the surface of the metal catalysts in real time during deactivation and regeneration processes. This approach enables a comprehensive evaluation of catalyst availability and offers valuable insights into deactivation and regeneration mechanisms. Such knowledge can be used to develop strategies to optimize catalyst performance and extend their lifetime, as well as to recover deactivated noble metal catalysts. Implementing such an approach ensures a more efficient and sustainable utilization of these valuable catalysts, thereby contributing to a greener future.

Techniques for obtaining coke-related information can be broadly categorized into optical and non-optical methods. Conventionally, coking information has been obtained by analyzing used catalyst extracted from reaction chambers through combustion or high-temperature analysis techniques such as temperature programmed oxidation[18,19], differential thermal analysis[20,21], and thermogravimetric analysis[22–24]. Vacuum-based techniques, such as X-ray photoelectron spectroscopy and secondary ion mass spectrometry, are also commonly utilized to investigate catalyst coking and other forms of poisoning[23–25]. However, these techniques typically do not offer spatially resolved information about coke formation. To address this limitation, advanced microscopy techniques, such as hyperspectral confocal fluorescence microscopy combined with tip-enhanced fluorescence microscopy, have been developed to directly investigate the surface coke formation[15]. Transmission electron

[1]Leibniz Institute of Photonic Technology, Albert-Einstein-Str. 9, 07745 Jena, Germany. [2]Institute of Physical Chemistry and Abbe Center of Photonics, Friedrich Schiller University Jena, Helmholtzweg 4, 07743 Jena, Germany. [3]Department of Chemistry, National Taiwan University, No. 1, Sec. 4, Roosevelt Rd., Taipei, 10617, Taiwan. [4]Institute of Solid State Physics, Friedrich Schiller University Jena, Helmholtzweg 3, 07743 Jena, Germany. [5]Research Center for Applied Sciences, Academia Sinica, 128 Sec. 2, Academia Rd., Taipei, 11529, Taiwan. [6]Department of Electrophysics, National Yang Ming Chiao Tung University, No. 1001, University Rd., Hsinchu, 30010, Taiwan. ✉e-mail: yi.ju.chen@uni-jena.de; jer-shing.huang@leibniz-ipht.de

microscopy (TEM) and scanning electron microscopy (SEM), often coupled with energy-dispersive X-ray spectroscopy, are also widely used for detailed analysis of coke morphology, crystalline structure, and elemental composition[23,24].

Optical techniques, such as spectroscopic ellipsometry, can determine film thickness and refractive index, while optical transmission and reflection measurements are commonly used to determine thin film thickness[26]. In addition, optical sensing, which integrates light sources and sensors with optical fibers, enables signal transmission and in-situ data collection. These systems can operate under extreme conditions, such as high temperatures and pressures, making them suitable for coke detection[27,28].

However, these optical methods typically require a stable light source, a flat and large sample surface and a bulky spectrometer, making it difficult to monitor the coking layer on microelectrodes. Moreover, a reference beam is necessary to remove the effect of the source intensity fluctuation, rendering the evaluation of the complex refractive index and thickness of extremely thin or non-transparent thin films challenging. For extremely thin films, the interference fringes are not pronounced. As a result, the fitting procedures may yield multiple solutions, which makes quantitative analysis difficult[29]. Most of the methods mentioned above are either invasive to the sample, or require post-data analysis, making them unsuitable for reliable and continuous on-site monitoring of the coking process[15,18,30,31]. Currently, no efficient methods are available for providing non-destructive and on-site quantitative results for coke detection.

To address this issue, we exploit our previous design of plasmonic azimuthally chirped gratings (pACGs)[32–36], also called plasmonic Doppler gratings, and introduce the so-called dielectric-loaded plasmonic azimuthally chirped gratings (DL-pACGs) for coke detection, as illustrated in Fig. 1a. Dielectric-loaded plasmonic devices do not require the plasmonic metallic substrate to be structured. The morphology of the devices is purely determined by the loaded dielectric structure, while the plasmonic metal remains flat and continuous. This flat metal layer mimics realistic conditions, such as those found on catalytic metal surfaces. This configuration enables non-destructive, on-site monitoring of coke thickness on the metal catalyst surface. A further advantage of the DL-pACGs for coke detection lies in its image-based analysis, which allows for spectrometer-free optical detection of coking, independent of fluctuations in source power or detector sensitivity. This innovative approach provides a reliable and straightforward method for coke detection and holds strong potential for in-situ, real-time optical monitoring of coking phenomena on heterogeneous catalysts. Furthermore, our DL-pACGs can also be adapted to incorporate actively tunable materials in place of PMMA, allowing for dynamic control of the working window in response to external stimuli such as temperature, humidity, pH, or ionic strength. As mentioned, this approach enables spectroscopic analysis without the need for additional far-field dispersive optical elements, like prisms. All these advantages make our pACGs platform particularly well-suited for microfluidic devices and lab-on-a-chip systems. This adaptability positions it as an excellent option for portable, on-site analytical tools.

The DL-pACGs used in this work is a PMMA grating structure with azimuthally varying periodicities, placed on top of the coked gold (Au) surface, as shown in Fig. 1a. The thin carbon layer, with a thickness ranging from 0 to 25 nm, placed between the structured PMMA layer and the Au substrate, significantly affects the reflection intensity profile as a function of the azimuthal angle. Briefly, this design features a series of eccentrically configured circular rings that create a continuous azimuthally varying lattice momentum. The eccentric spatial configuration of rings is designed in such a way that the trajectory of the nth ring can be described as,

$$(x - nd)^2 + y^2 = (n\Delta r)^2 \tag{1}$$

In Eq. (1), Δr represents the increment in ring radius and d represents the shift in the center of the rings. The continuum of azimuthal angle-dependent periodicity ranges from $\Delta r - d$ to $\Delta r + d$, corresponding to azimuthal angles of 180° and 0°, respectively. The mathematical relationship between the grating periodicity (P) and the azimuthal angle (ϕ) is given by,

$$P(\phi) = \pm d\cos\phi + \sqrt{\frac{d^2\cos 2\phi + 2\Delta r^2 - d^2}{2}} \tag{2}$$

This design allows for a range of momentum-matching possibilities between the incident light and surface plasmon polaritons (SPPs) through the periodicity-dependent grating momentum. The condition for momentum matching can be expressed as[32]:

$$\frac{2\pi}{\lambda_0} n_{eff}\sin\alpha + \frac{2m\pi}{P(\phi)} = \pm\frac{2\pi}{\lambda_0}\sqrt{\frac{\varepsilon_m n_{eff}^2}{\varepsilon_m + n_{eff}^2}} \tag{3}$$

where λ_0 represents the wavelength of the incident light, α is the angle of incidence, n_{eff} is the effective local refractive index of the surroundings, ε_m is

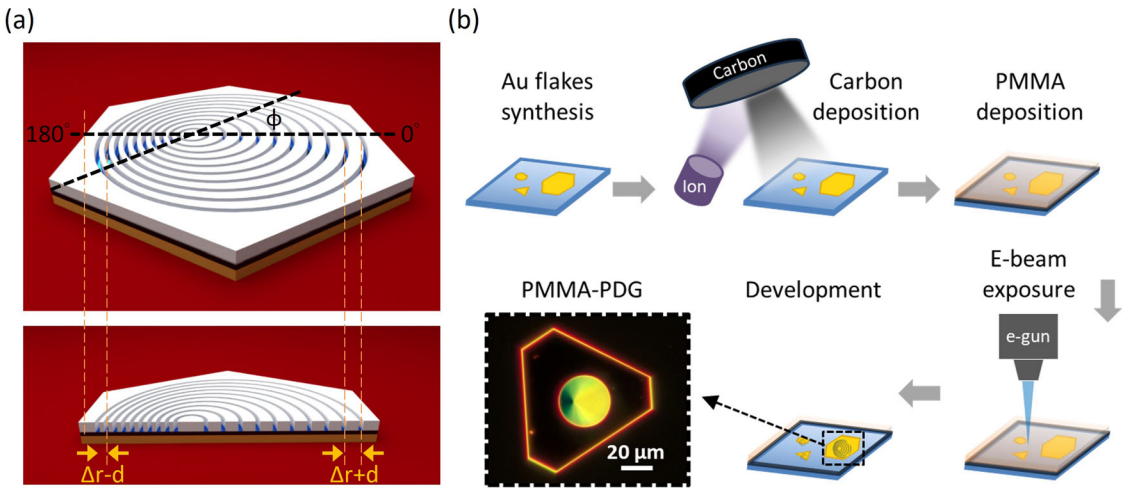

Fig. 1 | Structural design and fabrication of DL-pACGs. a Schematic illustration of the DL-pACGs structure, where d is 250 nm and Δr is 600 nm. The grating period varies continuously with the in-plane azimuthal angle (φ), from the largest value ($\Delta r + d$) at $\phi = 0°$ to the smallest value ($\Delta r - d$) at $\phi = 180°$. The thickness of PMMA (white) is 100 nm, carbon (black) ranges from 0 to 25 nm, and Au (yellow) is 100 nm. (**b**) Schematic of the sample fabrication process. The inset in (**b**) shows a representative dark-field image of a DL-pACGs on a truncated hexagonal Au flake from this work.

the permittivity of the metal, m is the resonant order, and P is the periodicity. The term $\frac{2\pi}{\lambda_0} n_{eff} \sin\alpha$ corresponds to the momentum of the incident light, $\frac{2\pi}{P(\phi)}$ represents the azimuthal angle-dependent grating momentum, and $\pm \frac{2\pi}{\lambda_0}\sqrt{\frac{\varepsilon_m \cdot n_{eff}^2}{\varepsilon_m + n_{eff}^2}}$ indicates the momentum of the surface plasmon polaritons propagating on the metal surface. SPPs propagate along the Au/carbon interface, with evanescent fields extending tens to hundreds of nanometers into the surrounding layers, including carbon, PMMA and air. Therefore, the n_{eff} is determined by the local dielectric environment defined by these adjacent layers, which is a combination of the refractive indices of the PMMA ($n_{PMMA} = 1.49$)[37], carbon ($n_{carbon} = 2.2–3.0$), and air ($n_{air} = 1$). The refractive index of carbon ranges from 2.2 to 3.0 in the visible region, depending on the thickness and internal morphology of the amorphous carbon layer[38,39].

Regarding Eq. (3), we recognize that the dynamic range of the index sensor can be tuned by selecting an appropriate range of grating periodicities. However, the momentum-matching condition does not consider structural parameters such as the grating's width, length, and height. Additionally, because the dielectric properties of thin carbon films depend nonlinearly on thickness, deriving a simple closed-form analytical expression that includes thickness as a variable is not straightforward. Therefore, we use refractive index data for carbon obtained from ellipsometry measurements and apply finite-difference time-domain (FDTD) simulations to model and validate how carbon thickness influences the angular reflection profile. The optimized design was fabricated on the surface of multiple monocrystalline gold flakes coated with carbon layers ranging from 0 to 25 nm in thickness to simulate coking conditions. The parameter scan used for structural optimization is shown in Fig. S1.

According to Eqs. (2) and (3), the optical response of the DL-pACGs, including the central wavelength and the span of the operational spectral window, can be freely designed by selecting appropriate values of Δr and d. For a given grating structure, a change in the refractive index of the surroundings (n_{eff}) would lead to a change in the momentum matching condition and thus the periodicity for light-surface plasmon coupling. Experimentally, the observed angular profile of the reflection intensity, specifically the dark band in the reflection image, varies with the surrounding refractive index, making the system an effective, spectrometer-free index sensor[33,35].

In this work, thin amorphous carbon films with various thicknesses ranging from 0 to 25 nm were prepared and examined using an ellipsometer to obtain thickness-dependent values of complex permittivity for the simulations, which provides the expected intensity angle profile for a specific carbon layer thickness to be compared with experimental results. The carbon layer was deposited via ion-beam deposition, and the DL-pACGs structure was patterned using electron-beam lithography. Additional fabrication details are provided in the Experimental Section. Figure 1b shows the schematic of the fabrication process and the dark-field image of the well-fabricated DL-pACGs. It is noteworthy that the color distribution observed on the DL-pACGs reflects the dispersive properties of our design.

Results

Determining the optical constants of carbon films using Ellipsometry

In this work, we aimed to address the issue of coke layers with thicknesses in the 0–25 nm range, which have been reported to cause catalytic deactivation. Since the optical characteristics of thin carbon films vary with the thickness[38,39], our initial step involved utilizing ellipsometry to determine the refractive index of these thin carbon films. In the following text, the thickness specified during film preparation is referred to as the nominal thickness, while the values obtained from ellipsometry fitting are referred to as the modeled thickness.

The complex dielectric permittivity ε has been derived mathematically by fitting oscillator functions to the measured dispersive ellipsometry parameters Ψ and Δ for amorphous carbon thin films with nominal thickness ranging from 5 nm to 25 nm. For each carbon thin film, Ψ and Δ were measured and fitted with oscillator functions over the spectral range of 210 nm to 1000 nm and under multiple angles of incidence (20° to 55° with a regular increment of 5°). The real and imaginary parts of ε, i.e., ε_1 and ε_2 respectively, are causally interlinked due to the preservation of Kramers-Kronig consistency[40–42]. The optical constants n and k can be calculated from ε_1 and ε_2 by employing the following mathematical relations[42].

$$n = \frac{1}{\sqrt{2}} \times \sqrt{\varepsilon_1 + \sqrt{\varepsilon_1^2 + \varepsilon_2^2}} \tag{4}$$

$$k = \frac{1}{\sqrt{2}} \times \sqrt{-\varepsilon_1 + \sqrt{\varepsilon_1^2 + \varepsilon_2^2}} \tag{5}$$

The thin films under investigation were deposited on glass substrates. Therefore, a bare glass substrate was first measured with spectroscopic ellipsometry under multiple angles of incidence (20° to 70° with a regular increment of 5°) over a spectral range of 210 nm to 1000 nm. A model described by the Sellmeier equation was used to provide an accurate fit to the measured data for the transparent glass substrate with a mean squared error (MSE) of 0.692[43]. The optical constants of the glass substrate were kept constant for the subsequently fitted carbon-layer-on-glass-substrate models.

A general feature of amorphous carbon thin films is the simultaneous presence of conductive sp^2-hybridized clusters and insulating sp^3-hybridized clusters as well as clusters with a mixture of sp^2- and sp^3-hybridized carbon. Studies have reported an inverse relationship between the sp^2 carbon content and the optical band gap in amorphous carbon films[44]. In this work, the sp^2 carbon content is considered the primary factor contributing to the broad absorption feature of the amorphous thin films. The optical constants of each amorphous carbon thin film were modeled by fitting a single Lorentzian oscillator function to the experimental data measured under multiple angles of incidence (20° to 55° with a regular increment of 5°) over a spectral range of 210 nm to 1000 nm. The Lorentzian oscillator used to estimate ε_2 can be mathematically defined as follows:

$$\varepsilon_2 = \frac{A \cdot \Gamma \cdot E_0}{E_0^2 - E^2 - i \cdot E \cdot \Gamma} \tag{6}$$

Equation (6) consists of three fit parameters, i.e., A as the amplitude of the Lorentzian peak, Γ (eV) as the full width at half maximum (FWHM) of the Lorentzian peak and E_0 (eV) as the energy where ε_2 reaches its peak. In addition to the aforementioned Lorentzian parameters, the General Oscillator parameters that operate outside the spectral ranges from 210 nm to 1000 nm contribute to ε_1. These are the dielectric constant at infinite frequency or at very high energy (ε_∞)[45,46], the amplitude and energy (eV) of the zero-broadened or sharp Lorentzian features in the UV range (A_{UV} and E_{UV}, respectively), and the amplitude of the zero-broadened Lorentzian oscillator in the IR range (A_{IR}). The fitted oscillator parameters, modeled film thickness and MSE are provided for each carbon film in Table 1.

It is clear from the fitted parameters in Table 1, and the optical constants depicted in Fig. 2a and b that the model predicts an absorption peak in the wavelength range between 200 nm and 300 nm. This feature is consistent with the published literature on amorphous carbon materials[47,48]. A rigorous description of the intrinsic structural anisotropy of the thin amorphous carbon films is difficult to provide due to the lack of long-range order and orientation in the films. Contributions from cross-polarized and depolarized response would require a complete Mueller matrix analysis, thereby leading to further complexity in the model. Such analysis would also be subject to variations depending on the local structure of the particular amorphous film being characterized. Our ellipsometric analysis in conjunction with FDTD simulations, on the other hand, aims to provide a simple yet effective model for validating the capability of DL-pACGs to monitor carbonaceous deposits that may compromise the efficiency of

various industrial processes. Finally, it is worth noting that the consistency with published literature along with the close alignment between the experimental results and the ellipsometric analysis-informed FDTD simulations, as shown later in Fig. 3, makes the case for the accuracy of our model.

Optical characterization and simulation of DL-pACGs

In the next step, we designed a DL-pACGs specifically tailored to measure coking layers with thicknesses below 25 nm on a gold surface. Using FDTD simulations, along with the refractive index and the modeled film thickness, we determined the optimal structural parameters for the DL-pACGs to operate within the visible spectral range. The grating features a radial increment (Δr) of 600 nm and a central displacement ($\boldsymbol{d}$) of 250 nm. The grating period ranges from 350 nm to 850 nm. The gap width is approximately 160 nm, with a PMMA thickness of 100 nm.

Table 1 | Oscillator parameters for various carbon thicknesses

Nominal Film Thickness (nm)	Lorentzian Parameters	General Oscillator Parameters	Modeled Film Thickness (nm)	MSE
5	A = 3.564 Γ = 27.956 E_0 = 8.597	ε_∞ = 1.000 A_{UV} = 5.000 E_{UV} = 10.000 A_{IR} = 5.000	3.97	0.514
10	A = 3.335 Γ = 25.899 E_0 = 8.837	ε_∞ = 1.000 A_{UV} = 5.000 E_{UV} = 10.000 A_{IR} = 5.000	9.68	0.640
15	A = 3.326 Γ = 26.385 E_0 = 8.832	ε_∞ = 1.000 A_{UV} = 5.000 E_{UV} = 10.000 A_{IR} = 5.000	14.60	0.694
20	A = 3.300 Γ = 25.783 E_0 = 9.114	ε_∞ = 1.000 A_{UV} = 5.000 E_{UV} = 10.000 A_{IR} = 5.000	19.63	0.813
25	A = 3.314 Γ = 26.602 E_0 = 9.090	ε_∞ = 1.000 A_{UV} = 5.000 E_{UV} = 10.000 A_{IR} = 5.000	24.08	0.756

To analyze the coking layer thickness, we examined the reflection images of the DL-pACGs using an upright microscope system (AxioScope A1, Zeiss). The observation was conducted in reflection mode under bright-field illumination. For the bright-field reflection images, we used white light illumination (HAL 100 illuminator with a quartz collector, Zeiss) along with a 532 nm bandpass filter (Thorlabs, FLH532-4) to provide green light. The incident light was directed through a 50X objective (N.A. = 0.7) onto the sample plane using Köhler illumination. The optical setup for the reflectance image measurement is depicted in Fig. 2(b).

In this setup, the white light source is first focused by the collector lens, forming an image onto the aperture diaphragm located in the vertical illuminator. The aperture diaphragm controls stray light and regulates the intensity of illumination without altering the size of the illuminated field. The light then passes through the field diaphragm, field lens, and bandpass filter to generate green light. It is subsequently reflected by a beamsplitter and focused onto the rear focal plane of the objective. The objective projects this light through the sample without focusing it, ensuring homogeneous illumination. Notably, the light source, aperture diaphragm, and the objective's rear focal plane form a conjugate plane illumination system. The light reflected from the sample surface is then collected by the objective and then directed to the CCD camera.

In the reflection images, dark bands show up at azimuthal angles where the grating's lattice momentum satisfies the momentum-matching condition. These dark bands stem from the coupling of light into surface plasmons which are of a near-field nature and thus cannot be detected in the far field. Since the coke thickness influences the local refractive index around the grating, according to Eq. (3), the suitable period for exciting SPPs at a specific wavelength and specific incident angle varies with the thickness, leading to a change in the azimuthal angles of the dark bands in the images. Therefore, the angles of the dark bands in the images can be used to determine the thickness of the coking layer, enabling image-based coking analysis, as illustrated in Fig. 3a. Under 532 nm illumination, the dark band shifts to a larger azimuthal angle as the nominal carbon thickness increases from 0 to 25 nm, with the modeled film thickness ranging from 0 to 24.08 nm.

The intensity distributions observed in the reflection images were translated into azimuthal intensity profiles, as shown in Fig. 3b, with the corresponding simulated results presented in Fig. 3c. The reflection dips, marked by red triangles, represent the azimuthal positions of the dark bands. As the carbon layer thickness increases, these reflection dips shift to larger azimuthal angles. The experimental results align well with the simulations,

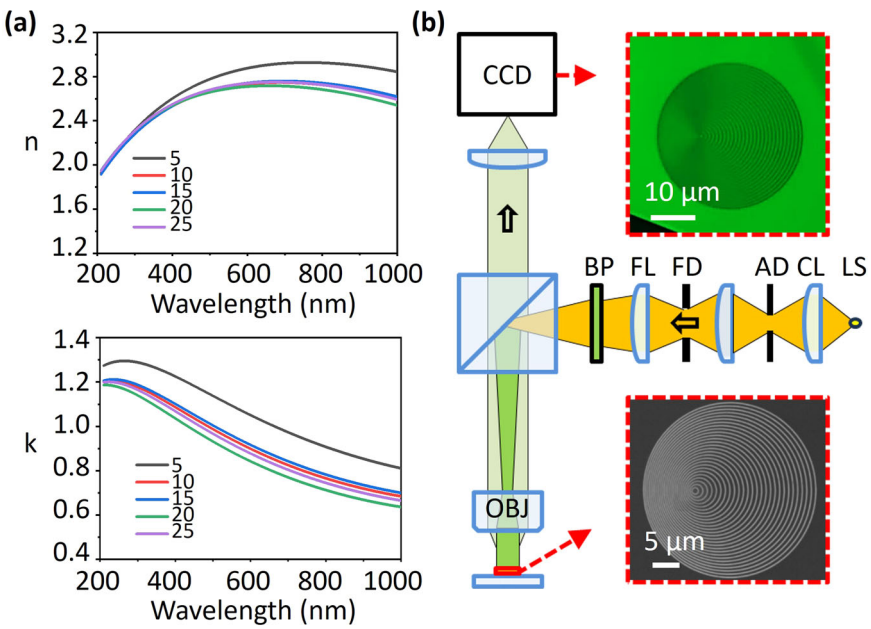

Fig. 2 | Ellipsometry characterization and optical imaging setup for DL-pACGs. a Ellipsometry characterization of the refractive index of thin carbon films with nominal thicknesses ranging from 5 to 25 nm, measured across a spectral range of 200 to 1000 nm. **b** Schematic of the optical setup used for capturing the reflectance image. Unpolarized white light from the light source (LS) first passes through the collector lens (CL), then enters the vertical illuminator, which includes an aperture diaphragm (AD), a lens, field diaphragms (FD), a field lens (FL), and a bandpass filter (BP). The light is then reflected by a beamsplitter and directed through the objective (OBJ) to illuminate the specimen under Köhler illumination. Reflected light from the specimen's surface re-enters the objective and is directed into the camera (CCD). The insets in **b** show a representative bright-field CCD image under green light illumination (upper inset) and SEM image (lower inset) of the DL-pACGs used in this work. The contrast in the SEM image comes from the difference in electron scattering efficiency of gold (bright) and PMMA (dark).

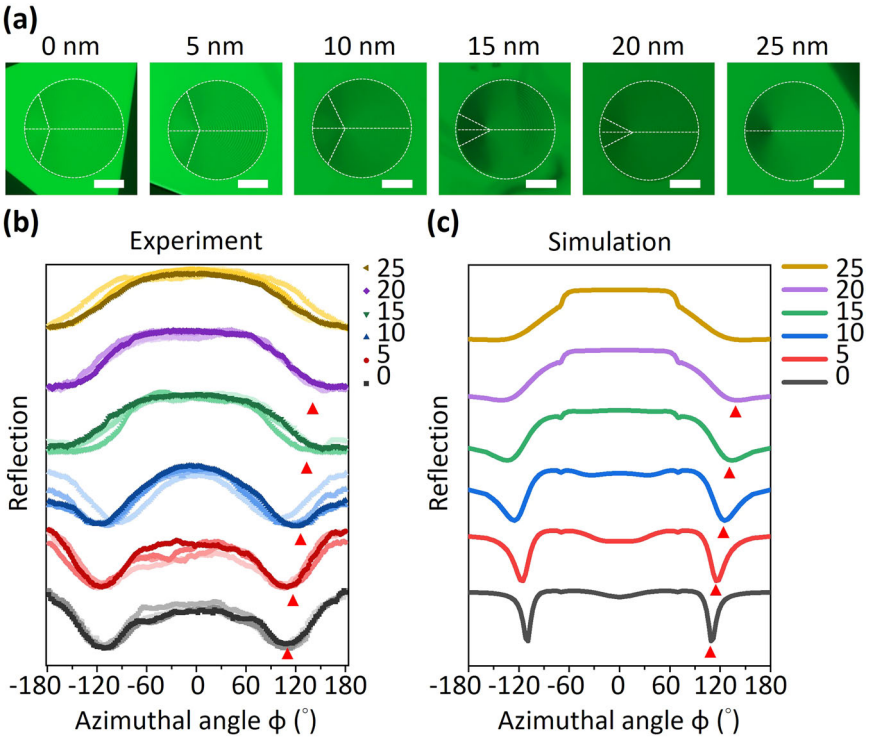

Fig. 3 | Experimental and simulated reflectance profiles of DL-pACGs under 532 nm illumination. **a** Reflectance CCD image of DL-pACGs with nominal carbon thicknesses ranging from 0 to 25 nm under 532 nm illumination. The scale bar, applicable to all images, is 10 μm. The CCD images reveal the variation in reflectance intensity with changes in the carbon layer thickness, illustrating the effect of carbon deposition on the optical response of the DL-pACGs. **b** Measured reflectance intensity profiles as functions of the azimuthal angle (ϕ) **c** Simulated reflectance intensity profiles obtained from FDTD calculations for the same DL-pACGs design. The red triangles indicate the angles corresponding to the dark bands, showing excellent agreement with the experimental measurements.

validating the underlying sensing principle. However, the experimental dips are broader and less sharp compared to the simulated ones. This discrepancy can be primarily attributed to structural imperfections in the fabricated gratings and the limited number of grating elements, in contrast to the ideal, perfectly periodic structures assumed in the simulations. To further investigate the resonance mechanism, the electric field distribution at the resonance wavelength was simulated for a DL-pACGs structure with a 5 nm carbon layer, as shown in Fig. S2 of the Supporting Information. The results reveal field confinement at the PMMA grating/carbon/Au interfaces, indicating the excitation of surface plasmon polaritons at the interface. This demonstrates that the plasmonic response is highly sensitive to variations in carbon layer thickness.

As mentioned in the introduction, most coke characterization techniques are destructive and require post-analysis procedures, which makes them unsuitable for real-time, on-site analysis. On the other hand, non-destructive spectroscopic techniques used for film characterization typically rely on a stable light source and a spectrometer. However, these methods face challenges when dealing with very thin or highly absorbent films. Thin films can lead to ambiguous or multiple solutions during data fitting, while highly absorbent films may produce little to no signal. Our approach addresses these limitations by focusing on angular position rather than intensity. This image-based angular analysis naturally avoids issues that could introduce noise or uncertainty in intensity measurements, such as fluctuations in source intensity or variations in the quality and thickness of the gold film, making it a promising method for in-situ and real-time coking monitoring. Furthermore, the issue of high absorbance in carbon-based materials, such as graphite and amorphous carbon, is effectively minimized in our DL-pACGs design. This approach is both simple and efficient, overcoming the limitations of traditional methods. It is non-destructive, making it ideal for on-site detection, and eliminates the need for bulky spectrometers or stable light sources.

A calibration curve relating azimuthal angle to carbon film thickness was established based on the simulated peak positions, as shown in Fig. 4, enabling quantitative determination of unknown coke thickness. In parallel, the azimuthal angles extracted from the experimental reflection images were plotted for comparison. For each carbon thickness, four data points were collected from DL-pACGs samples fabricated under identical conditions on coked gold surfaces.

Some deviation between the experimental and simulated trends is observed, which can be attributed to several factors. First, the simulations are based on ideal nanostructures with perfect geometry and material properties, whereas the fabricated samples may exhibit surface roughness or structural imperfections. These imperfections can lead to shifts or broadening of the dark bands in the reflection profiles. Second, limitations in microscope resolution or the finite number of pixels on the CCD may reduce the ability to resolve sharp intensity gradients or well-defined dips, resulting in broader features in the experimental data. Third, unpolarized light was used in the experiment, while the simulations assume p-polarized light, which couples more efficiently to surface plasmon modes. The presence of s-polarized components in the illumination may introduce additional coupling at slightly different azimuthal angles, leading to broader and slightly shifted features in the experimental profiles. Additionally, due to the finite size of the aperture diaphragm, the illumination beam is not perfectly collimated along the surface normal but spans a finite angular range. As a result, the dark band appears over a range of azimuthal angles rather than at a single angle. The shaded regions in the background of Fig. 4 represent the estimated range of azimuthal angles corresponding to illumination angle ranges of 0–5° and 5–10°, respectively. These ranges were calculated using Eq. (3). Despite these differences, the experimental trend shows good agreement with the simulation results, further confirming the effectiveness of the DL-pACGs in detecting nanoscale carbon layers.

Discussion

We have demonstrated the use of DL-pACGs for non-destructive monitoring of coking layer thickness from 0 to 25 nm. By analyzing the azimuthal angle of dark bands in the reflection images of DL-pACGs on gold surfaces coated with carbon layers of various thicknesses, we established a clear correlation between coke loading and the surface plasmon coupling angle. The position of the reflection minimum shifts with increasing carbon thickness due to the thickness-dependent change in the surrounding

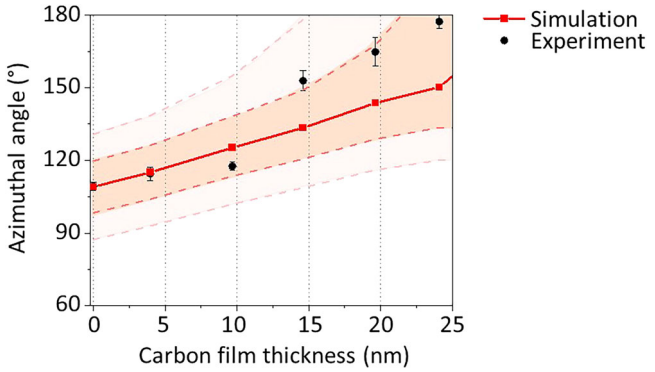

Fig. 4 | Calibration of carbon layer thickness via azimuthal dark-band angles in DL-pACGs. Calibration curve showing the relationship between carbon layer thickness and the azimuthal angles corresponding to the dark bands. The red line with square markers represents the azimuthal angles predicted by simulations, while the circular data points with error bars indicate the experimentally measured values. Note that the plotted data are based on the modeled film thicknesses obtained from ellipsometry. The shaded regions indicate the expected angular spread of the reflection dip due to the finite illumination cone, as estimated using Eq. (3). The orange region corresponds to an incident angle range of 0–5°, and the pink region corresponds to 5–10°.

refractive index, which directly influences the plasmonic coupling condition. This makes our approach a simple, image-based, and non-destructive method for monitoring coke accumulation on gold surfaces. Since the analysis is based on angular position rather than intensity, it avoids issues related to source intensity fluctuations and variations in metal surface quality, addressing major challenges associated with conventional absorption- or transmission-based intensity sensors.

It should be noted, however, that the current design does not yet have the resolution to precisely measure film thicknesses below 5 nm. The reasons for this limitation are two-fold. First, in this regime, the measurement uncertainty of ellipsometry becomes comparable to the film thickness itself. This means that although ellipsometry can still provide thickness estimates, it would need to be combined with appropriate optical models and cross-validated with high-resolution techniques such as TEM or X-ray reflectivity. Second, the dark bands in the reflection images of the current grating design have a relatively large azimuthal bandwidth, leading to a rather large uncertainty in determining the azimuthal angle. This limitation could be overcome by exploiting Fano resonance to create a sharp edge in the spatial profile of the reflected light. The Fano resonance can be optimized through the interference between localized resonances and the surface-lattice resonance of the grating[35,49,50]. Moreover, for carbon layers thinner than ~2 nm, quantum and nonlocal effects are expected to become significant, but incorporating such corrections would add complexity beyond the scope of this work.

Although the current study does not yet implement real-time or on-site coke sensing, our results demonstrate the foundational capability of the DL-pACGs platform for thin-film thickness monitoring. As the next step, we plan to integrate the DL-pACGs structure onto a fiber tip to enable in-situ, real-time monitoring under practical conditions. This integration is expected to provide a robust and compact sensing platform, offering an efficient and non-destructive tool for monitoring catalytic systems. The resulting system would be well-suited for both research and industrial applications. Future work will focus on sensor miniaturization, integration with portable light sources and detectors, and automated data acquisition to realize a real-time, on-site diagnostic system.

Methods

Simulation

We used the finite-difference time-domain method (Ansys Lumerical FDTD, Ansys) to simulate both the far-field spectrum and near-field distribution. Our two-dimensional numerical simulations were conducted on the cross-sectional planes of PMMA gratings placed on carbon and gold surfaces. By varying the grating periodicity, we simulated the reflection spectrum at corresponding azimuthal angles. The dimensions of the grating structure were derived from SEM images of the actual DL-pACGs. The PMMA grating has a height of 100 nm, with periodicities ranging from 350 to 850 nm and a grating gap of approximately 160 nm. The thickness and refractive index of the carbon layer were obtained from ellipsometry measurements.

A polarized total-field scattered-field plane wave source is injected from the air with a normal incidence angle, simulating the experimental conditions of single-wavelength bright-field illumination. The reflectance spectra were obtained by integrating the Poynting vector over a one-dimensional linear monitor placed 900 nm above the PMMA surface in the air. To analyze the resonance modes, we recorded the cross-sectional near-field profile at the resonance of the DL-pACGs using a two-dimensional monitor that extends over the air, PMMA, carbon, and gold layers. The mesh step was set to 2 nm in the x direction and 10 nm in the y direction within the volume covering the pACGs.

Synthesis of Au flakes

Before synthesizing Au flakes, it's crucial to thoroughly clean the centrifuge tubes and coverslips. The synthesis procedure involved introducing 10 mL of ethylene glycol (EG, Acros Organics, 99.5%) and 90 µL of a 0.1 M chloroauric acid ($HAuCl_4{\cdot}3H_2O$, Alfa Aesar, 99.99%) solution into the centrifuge tube. The tube was then gently shaken by hand to ensure proper mixing. A clean coverslip was subsequently placed inside the tube to serve as the substrate for flake growth. Once the coverslip was in place, the tube was sealed and positioned vertically in an oven. The reaction occurred consistently at 95 °C for 24 h. The size of the resulting flakes could be modulated by adjusting the baking time. After the synthesis period was complete, the coverslip containing the Au flakes was removed from the tube and immersed in ethanol. It was gently shaken to eliminate any residual EG. This cleaning procedure was repeated three times to ensure thorough removal of impurities.

DL-pACGs fabrication

We first deposited carbon layers, ranging from 5 to 25 nm in thickness, onto the selected crystalline Au flakes using ion beam deposition (Multiplas II). Subsequently, a 100 nm layer of PMMA (ARP617.03, Allresist) was spin-coated at 3000 rpm and annealed for 10 minutes at 200 °C. The pACGs structure was then inscribed onto the PMMA film using an e-beam (Vistec LION-LV1, beam energy 20 keV). Afterward, the sample was immersed in a developer solution (MIBK: IPA = 1:3) for 30 seconds to eliminate the areas exposed by the e-beam writing tool. Following the development procedure, our DL-pACGs structure was successfully fabricated on the carbon/Au substrate.

Carbon deposition and thickness control

The carbon layers in our study were deposited using Ion Beam Deposition (IBD). To determine the deposition rate, we first performed a longer test coating, from which the rate was measured to be approximately 1.3 nm/min. Based on this rate, the desired carbon thicknesses were obtained by adjusting the deposition time accordingly. To verify the thickness of the test coating, we used a Dektak surface profilometer. This measurement was performed immediately prior to the actual deposition of the experimental samples and served to calibrate the coating times. An uncertainty of less than 8% has been demonstrated, corresponding to approximately ±2 nm at a nominal thickness of 25 nm, with a general trend of decreasing uncertainty at lower nominal thicknesses. This suggests that the nominal thickness of the films is very accurate. Then the actual carbon thickness used in the optical simulations was further refined through ellipsometry measurements. By fitting the ellipsometry data to an optical model, we obtained what we refer to as the "modeled film thickness."

Ellipsometry measurement and analysis

The spectroscopic ellipsometry measurements were carried out in reflection mode using a J.A. Woollam RC2 ellipsometer. The ellipticity of the reflected light produced upon interaction of linearly polarized incident light with each amorphous carbon thin film deposited on glass substrate was measured over a spectral regime ranging from 210 nm to 1000 nm[51,52]. In order to arrive at very accurate results, our measurements were conducted under multiple angles of incidence ranging from 20° to 55° with a regular increment of 5° for each amorphous carbon thin film. The Lorentz oscillator was used to create a model which was then fit to the broadband spectra measured under multiple angles of incidence, using the CompleteEASE software from J.A. Woollam, to accurately extract the corresponding optical constants for each carbon film. Once a high degree of accuracy in the fit was achieved over the entire spectral regime at every angle of incidence for a carbon film of a certain thickness, the corresponding optical constants were calculated from the oscillator function. Over the entire process, a constant Sellmeier equation-based fit of the ellipsometry data measured from a bare glass substrate was used and only the model for the carbon film was varied with changing thickness.

Data availability

The data that support the findings of this study are available from the corresponding author upon reasonable request.

Received: 15 April 2025; Accepted: 1 September 2025;
Published online: 28 October 2025

References

1. Wu, X.-F., Anbarasan, P., Neumann, H. & Beller, M. From noble metal to Nobel Prize: Palladium-catalyzed coupling reactions as key methods in organic synthesis. *Angew. Chem. Int. Ed.* **49**, 9047–9050 (2010).
2. Kumar, A., Choudhary, P., Kumar, A., Camargo, P. H. C. & Krishnan, V. Recent advances in plasmonic photocatalysis based on TiO2 and noble metal nanoparticles for energy conversion, environmental remediation, and organic synthesis. *Small* **18**, 2101638 (2022).
3. Zhou, X., Liu, G., Yu, J. & Fan, W. Surface plasmon resonance-mediated photocatalysis by noble metal-based composites under visible light. *J. Mater. Chem.* **22**, 21337–21354 (2012).
4. Vickers, J. W., Alfonso, D. & Kauffman, D. R. Electrochemical carbon dioxide reduction at nanostructured gold, copper, and alloy materials. *Energy Technol.* **5**, 775–795 (2017).
5. Ringe, S. et al. Double layer charging driven carbon dioxide adsorption limits the rate of electrochemical carbon dioxide reduction on Gold. *Nat. Commun.* **11**, 33 (2020).
6. Dunwell, M. et al. The central role of bicarbonate in the electrochemical reduction of carbon dioxide on gold. *J. Am. Chem. Soc.* **139**, 3774–3783 (2017).
7. Heck, K. N., Garcia-Segura, S., Westerhoff, P. & Wong, M. S. Catalytic converters for water treatment. *Acc. Chem. Res.* **52**, 906–915 (2019).
8. Farrauto, R. J. & Heck, R. M. Catalytic converters: state of the art and perspectives. *Catal. Today* **51**, 351–360 (1999).
9. Kašpar, J., Fornasiero, P. & Hickey, N. Automotive catalytic converters: current status and some perspectives. *Catal. Today* **77**, 419–449 (2003).
10. Mazumder, V., Lee, Y. & Sun, S. Recent development of active nanoparticle catalysts for fuel cell reactions. *Adv. Funct. Mater.* **20**, 1224–1231 (2010).
11. Faur Ghenciu, A. Review of fuel processing catalysts for hydrogen production in PEM fuel cell systems. *Curr. Opin. Solid State Mater. Sci.* **6**, 389–399 (2002).
12. Zhang, Y. et al. Recent advances in one-dimensional noble-metal-based catalysts with multiple structures for efficient fuel-cell electrocatalysis. *Coord. Chem. Rev.* **450**, 214244 (2022).
13. Vogt, E. T. C. & Weckhuysen, B. M. Fluid catalytic cracking: recent developments on the grand old lady of zeolite catalysis. *Chem. Soc. Rev.* **44**, 7342–7370 (2015).
14. Boskovic, G. & Baerns, M. *Basic Principles in Applied Catalysis* (ed. M. Baerns) 477–503 (Springer Berlin Heidelberg, Berlin, Heidelberg; 2004).
15. Bienz, S. et al. Probing coke formation during the methanol-to-hydrocarbon reaction on zeolite ZSM-5 catalyst at the nanoscale using tip-enhanced fluorescence microscopy. *Catal. Sci. Technol.* **12**, 5795–5801 (2022).
16. Espinat, D., Freund, E., Dexpert, H. & Martino, G. Localization and structure of carbonaceous deposits on reforming catalysts. *J. Catal.* **126**, 496–518 (1990).
17. Wan, Z., Li, G. K., Wang, C., Yang, H. & Zhang, D. Relating coke formation and characteristics to deactivation of ZSM-5 zeolite in methanol to gasoline conversion. *Appl. Catal. A: Gen.* **549**, 141–151 (2018).
18. T. Cao, A. N. et al. Insight into the role of material basicity in the coke formation and performance of Ni/Al_2O_3 catalyst for the simulated-biogas dry reforming. *J. Energy Inst.* **108**, 101252 (2023).
19. Ochoa, A. et al. Coking and sintering progress of a Ni supported catalyst in the steam reforming of biomass pyrolysis volatiles. *Appl. Catal. B: Environ.* **233**, 289–300 (2018).
20. Grimmer, C. et al. Description of steam cracker fouling and coking residues by thermal analysis-photoionization mass spectrometry. *Energy Fuels* **33**, 11592–11602 (2019).
21. Ren, Y., Mahinpey, N. & Freitag, N. Kinetic model for the combustion of coke derived at different coking temperatures. *Energy Fuels* **21**, 82–87 (2007).
22. Guichard, B. et al. Characterization of aged hydrotreating catalysts. Part I: Coke depositions, study on the chemical nature and environment. *Appl. Catal. A: Gen.* **367**, 1–8 (2009).
23. Singha, R. K. et al. Synthesis of highly coke resistant Ni nanoparticles supported MgO/ZnO catalyst for reforming of methane with carbon dioxide. *Appl. Catal. B: Environ.* **191**, 165–178 (2016).
24. Ochoa, A., Bilbao, J., Gayubo, A. G. & Castaño, P. Coke formation and deactivation during catalytic reforming of biomass and waste pyrolysis products: A review. *Renew. Sustain. Energy Rev.* **119**, 109600 (2020).
25. Schraut, A., Emig, G. & Sockel, H. G. Composition and structure of active coke in the oxydehydrogenation of ethylbenzene. *Appl. Catal.* **29**, 311–326 (1987).
26. Ylilammi, M. & Ranta-aho, T. Optical determination of the film thicknesses in multilayer thin film structures. *Thin Solid Films* **232**, 56–62 (1993).
27. Pendão, C. & Silva, I. Optical fiber sensors and sensing networks: overview of the main principles and applications. *Sensors* **22**, 7554 (2022).
28. Yan, M., Tylczak, J., Yu, Y., Panagakos, G. & Ohodnicki, P. Multi-component optical sensing of high temperature gas streams using functional oxide integrated silica based optical fiber sensors. *Sens. Actuators B: Chem.* **255**, 357–365 (2018).
29. Dirk, P. & Philippe Frederic, S. Methods for the determination of the optical constants of thin films from single transmission measurements: a critical review. *J. Phys. D: Appl. Phys.* **36**, 1850 (2003).
30. Koichumanova, K. et al. In situ ATR-IR studies in aqueous phase reforming of hydroxyacetone on Pt/ZrO2 and Pt/AlO(OH) catalysts: The role of aldol condensation. *Appl. Catal. B: Environ.* **232**, 454–463 (2018).
31. Bernauer, M. et al. Proton proximity – New key parameter controlling adsorption, desorption and activity in propene oligomerization over H-ZSM-5 zeolites. *J. Catal.* **344**, 157–172 (2016).
32. See, K.-M., Lin, F.-C. & Huang, J.-S. Design and characterization of a plasmonic Doppler grating for azimuthal angle-resolved surface plasmon resonances. *Nanoscale* **9**, 10811–10819 (2017).

33. Lin, F.-C. et al. Designable Spectrometer-Free Index sensing using plasmonic doppler gratings. *Anal. Chem.* **91**, 9382–9387 (2019).
34. Ouyang, L. et al. Spatially resolving the enhancement effect in surface-enhanced coherent anti-stokes Raman scattering by plasmonic Doppler gratings. *ACS Nano* **15**, 809–818 (2021).
35. Chen, Y.-J., Lin, F.-C., Singh, A. K., Ouyang, L. & Huang, J.-S. Spectrometer-free optical hydrogen sensing based on Fano-like spatial distribution of transmission in a metal−insulator−metal plasmonic Doppler grating. *Adv. Optical Mater.* **9**, 2100869 (2021).
36. Barman, P. et al. Nonlinear optical signal generation mediated by a plasmonic azimuthally chirped grating. *Nano Lett.* **22**, 9914–9919 (2022).
37. Beadie, G., Brindza, M., Flynn, R. A., Rosenberg, A. & Shirk, J. S. Refractive index measurements of poly(methyl methacrylate) (PMMA) from 0.4–1.6 µm. *Appl. Opt.* **54**, F139–F143 (2015).
38. Arakawa, E. T., Williams, M. W. & Inagaki, T. Optical properties of arc-evaporated carbon films between 0.6 and 3.8 eV. *J. Appl. Phys.* **48**, 3176–3177 (2008).
39. Anna, C. & Cosslett, V. E. The optical density and thickness of evaporated carbon films. *Br. J. Appl. Phys.* **8**, 374 (1957).
40. de, L. & Kronig, R. On the theory of dispersion of X-rays. *J. Opt. Soc. Am.* **12**, 547–557 (1926).
41. Kramers, H. A. La diffusion de la lumiere par les atomes. *Atti Cong. Intern. Fis. (Trans. Volta. Centenary Congr.) Como* **2**, 545–557 (1927).
42. Fujiwara, H. *Spectroscopic Ellipsometry: Principles and Applications.* (John Wiley & Sons, 2007).
43. Sellmeier, W. Ueber die durch die Aetherschwingungen erregten Mitschwingungen der Körpertheilchen und deren Rückwirkung auf die ersteren, besonders zur Erklärung der Dispersion und ihrer Anomalien. *Ann. der Phys.* **223**, 386–403 (1872).
44. Oppedisano, C. & Tagliaferro, A. Relationship between sp2 carbon content and E04 optical gap in amorphous carbon-based materials. *Appl. Phys. Lett.* **75**, 3650–3652 (1999).
45. Lyubimov, Y. A. Permittivity at infinite frequency. *Russ. J. Phys. Chem.* **80**, 2033–2040 (2006).
46. Cole, R. H. Dielectric Absorption in Polar Media and the Local Field. *J. Chem. Phys.* **6**, 385–391 (1938).
47. Li, Z. et al. Characterization of amorphous carbon films from 5 nm to 200 nm on single-side polished a-plane sapphire substrates by spectroscopic ellipsometry. *Front. Phys.* **10**, (2022).
48. Sathish-Kumar, K., Vázquez-Huerta, G., Rodríguez-Castellanos, A., Poggi-Varaldo, H. M. & Solorza-Feria, O. Microwave assisted synthesis and characterizations of decorated activated Carbon. *Int. J. Electrochem. Sci.* **7**, 5484–5494 (2012).
49. Kumar Singh, A. & Huang, J.-S. Optical responses of Fano resonators in non-spectral parametric domains. *Opt. Lett.* **47**, 3720–3723 (2022).
50. Chakraborty, A. et al. Broadband four-wave mixing enhanced by plasmonic surface lattice resonance and localized surface plasmon resonance in an azimuthally chirped grating. *Laser Photonics Rev.* **17**, 2200958 (2023).
51. Fujiwara, H. Introduction to Spectroscopic Ellipsometry. In *Spectroscopic Ellipsometry: Principles and Applications*, 1–11 (John Wiley & Sons, 2007).
52. Fujiwara, H. Principles of spectroscopic ellipsometry. In *Spectroscopic Ellipsometry: Principles and Applications,* 81–146 (John Wiley & Sons, 2007).

Acknowledgements

J.-S. H. acknowledges the support from DAAD (Projekt-ID: 57710865 and 57700890) and DFG (SFB-1375 NOA, Project No.: 398816777 and IRTG-2675 Meta-Active, Project No.: 437527638). H.K. acknowledges financial support from DFG (IRTG-2675 Meta-Active, Project No.: 437527638).

Author contributions

Y.-J.C. and T.-H.C. conceived and designed the study. U.H. and Y.-J.C. fabricated the samples. Y.-J.C. conducted optical characterization, image analysis, and numerical simulations. A.C. and S.V.V. measured and analyzed the carbon index under the supervision of H.K. J.-S.H. supervised the research. Y.-J.C., T.-H.C., and A.C. wrote the manuscript. All authors participated in discussions and contributed to manuscript revisions.

Competing interests

The authors declare no competing interests.

Additional information

Supplementary information The online version contains supplementary material available at https://doi.org/10.1038/s44310-025-00089-y.

Correspondence and requests for materials should be addressed to Yi-Ju Chen or Jer-Shing Huang.